Branch-dependent chaos bound behavior of spinning particles in a spherically symmetric black hole spacetime

Xiaowei Li (李小伟)[a†] Chuang Yang (杨创)[b‡] Deyou Chen (陈德友)[b§]

[a]School of Mathematics, Physics and Statistics, Sichuan Minzu College, Kangding 626001, China
[b]School of Science, Xihua University, Chengdu 610039, China

Abstract: We investigate the instability of spinning test particles and the associated classical chaos bound in a spherically symmetric black hole spacetime with two photon spheres. The radial effective potential admits two branches of unstable circular orbits in the near-horizon and far-horizon regions. Although both branches are locally unstable, their Lyapunov exponents have different relationships with the black hole surface gravity. The near-horizon branch satisfies the bound, whereas the far-horizon branch can violate it. We further examine the effects of particle spin, total angular momentum, and black hole parameters. Spin-curvature coupling shifts the unstable orbits and modifies their instability, whereas the total angular momentum and background parameters generally have larger effects. Our results show that the validity of the classical orbital chaos bound is branch dependent.

Keywords: spinning test particles, unstable circular orbits, classical chaos bound

DOI: 10.1088/1674-1137/aeaa13 **CSTR:** 32044.14.ChinesePhysicsC.51015107

I. INTRODUCTION

Chaos in thermal quantum systems can be diagnosed using out-of-time-order correlators (OTOCs), which probe the growth of initially small perturbations. In 2016, Maldacena, Shenker, and Stanford (MSS) conjectured that, for thermal quantum systems with many degrees of freedom and under the assumptions required for the analyticity and boundedness of the relevant correlator, this growth rate cannot exceed the temperature scale [1]

$$\lambda_L \leqslant 2\pi T, \tag{1}$$

where λ_L denotes a quantum Lyapunov exponent (LE), and natural units $k_B = \hbar = 1$ have been adopted. This inequality, known as the MSS chaos bound, sets a temperature-dependent upper limit on the exponent and has been widely discussed in black hole and holographic systems [2−4]. For rotating black holes, the situation is more involved because angular momentum introduces an additional chemical potential. In rotating BTZ spacetimes, Jahnke, Kim, and Yoon found that the left- and right-moving contributions to the OTOC are characterized by $\lambda_L^{\pm} = \frac{2\pi}{\beta}\frac{1}{1\mp\ell\Omega}$, where β is the inverse temperature, Ω is the black hole angular velocity, and ℓ is the AdS radius [5]. If both exponents are compared directly with the common scale $2\pi/\beta$, one of them can exceed this value. This can be reformulated in terms of the effective inverse temperatures $\beta_{\pm} = \beta(1\mp\ell\Omega)$. Poojary obtained a related result, finding $\lambda_L = 2\pi/\beta_+$, with $\beta_+ = \beta(1-\mu_L)$ and $\mu_L = r_-/r_+$ related to the angular momentum chemical potential [6]. The role of different modes in rotating BTZ spacetimes has also been examined using OTOCs, shock waves, and pole-skipping [7]. These studies show that the instability scale appearing in the OTOC can depend on the dynamical sector under consideration and that the angular momentum chemical potential must be treated carefully when discussing the chaos bound in rotating systems.

A related but physically distinct question arises for the local instability of classical particle trajectories outside a black hole. For an unstable circular orbit located at r_0, a small radial perturbation typically evolves as $\delta r(t) \sim \mathrm{e}^{\lambda t}$, where λ is a classical LE defined with respect to the coordinate time and characterizes the local exponential growth of radial perturbations around the unstable orbit. In natural units, the Hawking temperature T is related to the surface gravity κ by $T = \kappa/(2\pi)$. Thus, the thermal scale entering the MSS bound formally corresponds to the surface gravity scale. Although the OTOC LE and the LE governing classical orbital perturbations are physically distinct observables, this formal correspondence motivates the question of whether the surface

Received 1 August 2026; Accepted 20 September 2026; Accepted manuscript online 21 September 2026

† E-mail: xiaoweiliedu@hotmail.com
‡ E-mail: chuangyangyc@hotmail.com
§ E-mail: deyouchen@hotmail.com (Corresponding author)

©2027 Chinese Physical Society and the Institute of High Energy Physics of the Chinese Academy of Sciences and the Institute of Modern Physics of the Chinese Academy of Sciences and IOP Publishing Ltd. All rights, including for text and data mining, AI training, and similar technologies, are reserved.

gravity can also constrain the local instability of classical particle trajectories. In this context, Hashimoto and Tanahashi considered test particles maintained at unstable equilibrium positions near the horizon of a static, spherically symmetric black hole by electromagnetic or scalar forces. They showed that, in the near-horizon limit, the exponent associated with radial perturbations approaches the surface gravity, independently of the particle mass and of the detailed form and strength of the external force [8]. In the absence of additional sources of chaos, this result leads to the classical bound

$$\lambda \leqslant \kappa, \tag{2}$$

which is formally analogous to the MSS bound.

Zhao et al. subsequently revisited this result by retaining subleading terms in the near-horizon expansion. They found that the LE associated with radial perturbations approaches the surface gravity as the unstable equilibrium point approaches the event horizon. The bound is preserved in Reissner–Nordström (RN) and Reissner–Nordström–AdS (RN-AdS) spacetimes, but it can be violated in other black hole backgrounds [9]. Lei and Ge extended the analysis from static equilibria to circular motion of charged particles. Their results showed that the orbital angular momentum modifies both the radius of the unstable circular orbit and the curvature of the effective potential at the extremum. Consequently, the bound can be violated in RN, RN-AdS, and black brane spacetimes [10−13]. In rotating spacetimes [14−18], Gwak *et al*. further demonstrated that, although a negative cosmological constant generally suppresses the exponent, the combined effects of black hole rotation, particle charge, and orbital angular momentum can still lead to violations of the bound. Such violations become particularly pronounced in extremal and near-extremal configurations. Further studies of chaos-bound violations in black hole backgrounds can be found in [19−37]. These results indicate that the validity of the classical orbital bound depends on the relation between two characteristic scales: the surface gravity associated with the event horizon and the LE characterizing the local instability of the orbit. A universal relation between these scales is expected only in the near-horizon limit. At finite radius, the asymptotic structure of the spacetime, the black hole spin and proximity to extremality, and the charge and angular momentum of the particle can all alter the relation between the exponent and the surface gravity. This observation naturally motivates an examination of how spin–curvature coupling modifies the local instability of different unstable circular orbits and, consequently, their relation to the surface gravity scale.

Spinning test particles provide a useful probe of the role of spin–curvature coupling in local orbital instability and its relation to the surface gravity scale. Their motion is governed by the Mathisson–Papapetrou–Dixon (MPD) equations, in which the particle spin couples directly to the background curvature and modifies the effective radial dynamics. As a result, the locations and stability of circular orbits can depend on the spin magnitude and orientation, with spin–curvature coupling modifying the corresponding radial instability [38, 39]. The physically admissible spin range, however, must be treated with care. Excessively large spins can artificially amplify spin effects and invalidate the pole–dipole or test-particle approximations. It is therefore important to check the validity of these approximations when assessing possible violations of the chaos bound. Black hole spacetimes with multiple photon spheres provide an interesting setting for this problem [40−43]. Because photon spheres are defined by null geodesics, their existence does not imply a one-to-one correspondence with extrema of the effective potential for massive spinning particles, whose circular orbits must be determined independently from the MPD dynamics. For the parameter region investigated in the present work, the two unstable circular-orbit branches are already present in the spinless limit. Hence, spin–curvature coupling is not responsible for generating the two-branch structure; rather, it shifts the locations of the pre-existing orbits and modifies their local instability properties. Within the physically admissible spin range considered here, these corrections remain comparatively modest and do not create or eliminate either branch. Because the two branches correspond to different radial regions and different local curvatures of the effective potential, their LEs can exhibit different relations to the surface gravity.

Motivated by these considerations, we investigate the orbital instability of spinning test particles and its relation to the surface gravity scale in a black hole spacetime with two photon spheres. Our numerical analysis shows that, within an appropriate region of the black hole and particle parameter space, the radial effective potential possesses two well-separated local maxima, corresponding to near- and far-horizon unstable circular-orbit branches. We further examine how switching on the particle spin modifies these pre-existing branches. Within the physically admissible spin range considered, the particle spin modifies the orbital locations and local instability properties and, for the far-horizon branch, produces a modest shift in the critical boundary separating the bound-satisfying and bound-violating regions in the (S, L) parameter plane. We then compare the LE of each branch with the surface gravity to determine how its local instability depends on the orbital branch and spin–curvature coupling. Our aim is not to associate a chaos bound directly with the photon spheres themselves, but rather to examine how the nontrivial radial structure of the spacetime and spin–curvature coupling affect the local instability of the two unstable branches and their relation to the surface gravity scale.

The remainder of this paper is organized as follows. In Sec. II, we introduce a spherically symmetric black hole spacetime admitting two photon spheres, derive the equations of motion for a spinning test particle in this background, and define the corresponding LE. In Sec. III, we numerically investigate the local instability of unstable circular orbits and its relation to the surface gravity, with particular attention to the effects of the particle spin and the two orbital branches. Sec. IV presents the conclusion and discussion.

II. SPINNING PARTICLE DYNAMICS

A. Black hole geometry

We consider a four-dimensional gravitational theory that includes vector–tensor and scalar–tensor couplings to the Gauss–Bonnet term. The action is given by

$$\mathcal{S}=\int \mathrm{d}^4x\sqrt{-g}\left(R-\alpha\mathcal{L}_G^{\mathrm{VT}}-\beta\mathcal{L}_G^{\mathrm{ST}}\right), \tag{3}$$

$$\mathcal{L}_G^{\mathrm{VT}}=4G^{\mu\nu}W_\mu W_\nu+8(W_\rho W^\rho)\nabla_\mu W^\mu+6(W_\rho W^\rho)^2, \tag{4}$$

$$\mathcal{L}_G^{\mathrm{ST}}=\phi\mathcal{G}-4G^{\mu\nu}\nabla_\mu\phi\nabla_\nu\phi-4\Box\phi(\partial\phi)^2-2(\partial\phi)^4, \tag{5}$$

where $\mathcal{L}_G^{\mathrm{VT}}$ and $\mathcal{L}_G^{\mathrm{ST}}$ denote the vector–tensor and scalar–tensor Gauss–Bonnet contributions, respectively. The Gauss–Bonnet invariant is $\mathcal{G}=R^2-4R_{\mu\nu}R^{\mu\nu}+R_{\mu\nu\alpha\beta}R^{\mu\nu\alpha\beta}$ [44], and $G_{\mu\nu}=R_{\mu\nu}-\frac{1}{2}g_{\mu\nu}R$ is the Einstein tensor. The parameters α and β determine the coupling strengths of the vector–tensor and scalar–tensor Gauss–Bonnet terms, respectively.

A static, spherically symmetric black hole solution of this theory was obtained in [45, 46]. The corresponding line element is

$$\mathrm{d}s^2=-f(r)\mathrm{d}t^2+\frac{\mathrm{d}r^2}{f(r)}+r^2\left(\mathrm{d}\theta^2+\sin^2\theta\,\mathrm{d}\phi^2\right), \tag{6}$$

where the metric function reads

$$f(r)=1-\frac{2\alpha(M-Q)}{r(\alpha+\beta)}+\frac{r^2}{2(\alpha+\beta)}-\frac{r^2}{2(\alpha+\beta)}\sqrt{1+\frac{8\alpha Q}{r^3}+\frac{8\beta M}{r^3}-\frac{16\alpha\beta(M-Q)^2}{r^6}}. \tag{7}$$

Here, M denotes the black hole mass, whereas Q is an integration constant associated with the Proca field. Unlike a conserved charge associated with an asymptotic symmetry, Q represents a primary-hair parameter that characterizes the black hole solution. In the limit $M=Q$, Eq. (7) reduces to the black hole solution obtained from the scalar–tensor sector of four-dimensional Einstein–Gauss–Bonnet gravity [47]. When $\alpha=-\beta$, the metric function is

$$f(r)=\frac{r^3}{r^3-4\alpha(M-Q)}\left(1-\frac{2M}{r}+\frac{4\alpha(M-Q)^2}{r^4}-\frac{4\alpha(M-Q)}{r^3}\right). \tag{8}$$

In the numerical analysis below, we focus on the nondegenerate case $\alpha+\beta\neq0$ and use the metric function given in Eq. (7). Depending on the model parameters, this class of black hole solutions can admit two distinct photon spheres. This double-photon-sphere structure reflects the nontrivial radial geometry of the spacetime and can influence the propagation of null geodesics and the associated optical properties. It also provides the background for the orbital analysis considered below. For the metric in Eqs. (6), the surface gravity at the event horizon is

$$\kappa=\frac{f'(r_+)}{2}, \tag{9}$$

where the prime denotes differentiation with respect to r, and r_+ denotes the event horizon radius, determined by $f(r_+)=0$.

B. Conserved quantities and equations of motion

The dynamics of a spinning particle in curved spacetime can be described using the MPD formalism [48]. In the pole-dipole approximation, the equations governing the evolution of the particle's momentum and spin tensor are

$$\frac{D\tilde{p}^\mu}{D\tau}=-\frac{1}{2}R^\mu{}_{\nu\alpha\beta}u^\nu\tilde{S}^{\alpha\beta}, \tag{10}$$

$$\frac{D\tilde{S}^{\mu\nu}}{D\tau}=\tilde{p}^\mu u^\nu-u^\mu\tilde{p}^\nu, \tag{11}$$

where τ denotes the proper time along the particle trajectory, and $D/D\tau$ represents the covariant derivative with respect to τ. The quantities $\tilde{p}^\mu$ and $u^\mu=\mathrm{d}x^\mu/\mathrm{d}\tau$ denote the particle's four-momentum and four-velocity, respectively. The antisymmetric tensor $\tilde{S}^{\mu\nu}$ characterizes the intrinsic angular momentum of the particle, and $R^\mu{}_{\nu\alpha\beta}$ is the Riemann curvature tensor. The first MPD equation describes spin–curvature coupling, which causes the particle trajectory to deviate from the corresponding geodesic motion. The MPD equations have also been extended to the ultrarelativistic regime in [49].

The MPD equations contain redundant degrees of freedom due to the antisymmetric spin tensor. To specify the center-of-mass reference worldline of the spinning particle, an additional spin supplementary condition is re-

quired. Here, we adopt the Tulczyjew–Dixon (TD) supplementary condition [50, 51]

$$\tilde{S}^{\mu\nu}\tilde{p}_{\nu}=0, \tag{12}$$

which imposes orthogonality between the spin tensor and the particle four-momentum. The TD condition selects a representative centroid worldline and, together with the MPD equations, determines the relation between the four-velocity and the four-momentum. The particle mass m and spin magnitude $\tilde{S}$ are conserved quantities defined by $\tilde{p}^{\mu}$ and $\tilde{S}^{\mu\nu}$, respectively. For convenience, we introduce the normalized quantities

$$p^{\mu}=\frac{\tilde{p}^{\mu}}{m}, \qquad S^{\mu\nu}=\frac{\tilde{S}^{\mu\nu}}{m}, \qquad S=\pm\frac{\tilde{S}}{m}. \tag{13}$$

Here, S is a signed spin parameter, with $|S|$ denoting the normalized spin magnitude and its sign distinguishing the two possible spin orientations relative to the orbital angular momentum. Owing to spherical symmetry, the z axis is a coordinate choice and does not represent a physically preferred direction. For equatorial motion with the particle spin aligned or anti-aligned with the orbital angular momentum, the normalization conditions for the particle momentum and spin tensor reduce to

$$-1=p^{\mu}p_{\mu}=-(p^{t})^{2}f+\frac{(p^{r})^{2}}{f}+r^{2}(p^{\phi})^{2}, \tag{14}$$

$$S^{2}=\frac{1}{2}S^{\mu\nu}S_{\mu\nu}=-(S^{tr})^{2}-fr^{2}(S^{t\phi})^{2}+\frac{r^{2}(S^{r\phi})^{2}}{f}. \tag{15}$$

To investigate the orbital dynamics of a spinning particle around a black hole, we follow the approach developed in [38, 52], in which the equations of motion for neutral spinning particles in static, spherically symmetric spacetimes were systematically derived. The stationarity and axial symmetry of the spacetime imply two Killing vectors, $(\partial/\partial t)^{a}$ and $(\partial/\partial\phi)^{a}$, which yield two conserved quantities along the particle trajectory. The conserved energy $\tilde{E}=mE$ associated with the timelike Killing vector is given by

$$E=fp^{t}-\frac{1}{2}f'S^{tr}, \tag{16}$$

where the second term is the spin-dependent contribution to the conserved energy. Similarly, the axial Killing vector yields the conserved total angular momentum $\tilde{L}=mL$,

$$L=r^{2}p^{\phi}+rS^{r\phi}. \tag{17}$$

This quantity contains both orbital and spin contributions. For the circular-orbit configurations considered below, with $L>0$ and $p^{\phi}>0$, we adopt the convention that $S>0$ ($S<0$) denotes a particle spin aligned (anti-aligned) with the orbital angular momentum.

The TD supplementary condition can be written explicitly in the present spacetime as

$$\frac{p^{r}S^{tr}}{f}+r^{2}p^{\phi}S^{t\phi}=0, \tag{18}$$

$$r^{2}p^{\phi}S^{r\phi}+fp^{t}S^{tr}=0, \tag{19}$$

$$\frac{1}{f}p^{r}S^{r\phi}-fp^{t}S^{t\phi}=0. \tag{20}$$

Using the metric in Eq. (6), the MPD momentum equations can be expressed in terms of the independent dynamical variables as

$$\dot{p}^{t}+\frac{p^{r}f'}{2f}+\frac{\dot{r}p^{t}f'}{2f}-\frac{r\dot{\phi}S^{t\phi}f'}{2}-\frac{\dot{r}S^{tr}f''}{2f}=0, \tag{21}$$

$$\dot{p}^{r}+\frac{p^{t}ff'}{2}-\dot{\phi}p^{\phi}fr-\frac{r\dot{\phi}S^{r\phi}f'}{2}-\frac{S^{tr}ff''}{2}-\frac{\dot{r}p^{r}f'}{2f}=0, \tag{22}$$

$$\dot{p}^{\phi}+\frac{\dot{\phi}p^{r}}{r}+\frac{\dot{r}p^{\phi}}{r}+\frac{\dot{r}S^{r\phi}f'}{2fr}-\frac{S^{t\phi}ff'}{2r}=0. \tag{23}$$

Here, an overdot denotes differentiation with respect to coordinate time t. The corresponding evolution equations for the spin tensor, obtained from Eq. (11), are given by

$$\dot{S}^{tr}+p^{r}-\dot{r}p^{t}-fr\dot{\phi}S^{t\phi}=0, \tag{24}$$

$$\dot{S}^{t\phi}-\dot{\phi}p^{t}+p^{\phi}+\frac{\dot{\phi}S^{tr}+\dot{r}S^{t\phi}}{r}+\frac{S^{r\phi}f'+\dot{r}S^{t\phi}f'}{2f}=0, \tag{25}$$

$$\dot{S}^{r\phi}-\dot{\phi}p^{r}+\dot{r}p^{\phi}+\frac{\dot{r}S^{r\phi}}{r}+\frac{S^{t\phi}ff'}{2}-\frac{\dot{r}S^{r\phi}f'}{2f}=0. \tag{26}$$

By combining Eqs. (14)–(19) with the conserved quantities, the spin and momentum components can be expressed as

$$S^{tr}=-Srp^{\phi}, \tag{27}$$

$$p^{\phi}=\frac{L-ES}{r^{2}-\frac{1}{2}rS^{2}f'}, \tag{28}$$

$$p^t = \frac{2rE - SLf'}{(2r - S^2 f')f}. \tag{29}$$

Using Eqs. (28) and (29), together with the normalization condition (14), the radial component of the momentum is determined as

$$p^r = \pm\sqrt{p_t^2 - f\left(1 + \frac{p_\phi^2}{r^2}\right)}, \tag{30}$$

where $p_t = g_{tt}p^t$ and $p_\phi = g_{\phi\phi}p^\phi$. The two signs correspond to the two possible radial directions of particle motion: the positive branch describes an outward trajectory, whereas the negative branch represents an inward trajectory.

The radial effective potential plays a central role in evaluating the LE of the particle. Therefore, the radial equation of motion must be recast in terms of coordinate time. First, by combining the spin supplementary conditions given in Eqs. (18) and (19) with Eq. (15), the nonvanishing components of the spin tensor are obtained as

$$S^{t\phi} = \frac{Sp^r}{rf}, \tag{31}$$

$$S^{r\phi} = \frac{p^t S f}{r}. \tag{32}$$

By combining these relations with Eqs. (20) and (24), the following constraint equation is obtained:

$$\frac{(p^r - \dot{r}p^t)S^2 f'}{2r} - S(r\dot{p}^\phi + \dot{r}p^\phi) - p^r + \dot{r}p^t - \dot{S}^{tr} = 0. \tag{33}$$

By combining Eq. (33) with Eq. (27) and eliminating the spin-related terms through algebraic simplification, the radial and azimuthal velocities with respect to coordinate time are found to satisfy

$$\dot{r} = \frac{p^r}{p^t}, \tag{34}$$

$$\dot{\phi} = \frac{f p_\phi (2 - S^2 f'')}{r p_t (S^2 f' - 2r)}. \tag{35}$$

Although the angular equations of motion have been derived, we focus here on the radial dynamics because they govern the effective potential and determine the corresponding LEs analyzed below.

C. Radial instability and lyapunov exponent

The radial effective potential provides a convenient framework for analyzing the stability of particle trajectories and determining the corresponding LE. In particular, the LE is closely related to the curvature of the effective potential near an unstable equilibrium orbit [53]. Following the perturbative approach adopted in previous studies [25, 54], the radial equation in terms of coordinate time can be written as

$$\frac{1}{2}m\dot{r}^2 + \mathcal{V}_{\rm eff}(r) = 0, \tag{36}$$

where $\mathcal{V}_{\rm eff}$ denotes the effective potential. Using Eq. (34), the effective potential can be expressed as $\mathcal{V}_{\rm eff}(r) = -\frac{m}{2}\left(\frac{p^r}{p^t}\right)^2$. To investigate the instability of an unstable circular orbit at $r = r_0$, we introduce a small radial perturbation, $r(t) = r_0 + \epsilon(t)$. Expanding the effective potential around r_0 and retaining the leading-order terms yields the perturbation equation

$$\dot{\epsilon}^2 - \lambda^2\epsilon^2 = 0, \tag{37}$$

where the LE is determined from the second derivative of the effective potential [25, 54]

$$\lambda^2 = -\frac{\mathcal{V}''_{\rm eff}(r_0)}{m} = \frac{1}{2}\frac{{\rm d}^2}{{\rm d}r^2}\left(\frac{p^r}{p^t}\right)^2\bigg|_{r=r_0}. \tag{38}$$

A positive value of λ^2 indicates exponential growth of radial perturbations and thus signals orbital instability, whereas a negative value corresponds to stable radial motion.

For fixed black-hole parameters and particle parameters L and S, the conserved energy E is not prescribed independently. Instead, E and the circular-orbit radius r_0 are determined simultaneously for each parameter set from the conditions

$$\mathcal{V}_{\rm eff}(r_0; E) = 0, \tag{39}$$

$$\frac{\partial \mathcal{V}_{\rm eff}(r; E)}{\partial r}\bigg|_{r=r_0} = 0. \tag{40}$$

Here, the dependence of $\mathcal{V}_{\rm eff}$ on the fixed black hole and particle parameters is left implicit for notational simplicity. These two equations are solved simultaneously for the pair (E, r_0). Because the present analysis focuses on unstable circular orbits, the resulting solutions are further required to satisfy

$$\frac{\partial^2 \mathcal{V}_{\rm eff}(r; E)}{\partial r^2}\bigg|_{r=r_0} < 0, \tag{41}$$

This identifies r_0 as a local maximum of the radial effective potential and therefore corresponds to a circular orbit that is unstable to radial perturbations. In the subsequent analysis, we retain only physically admissible solutions that lie outside the event horizon, $r_0 > r_+$, and satisfy the constraints associated with spinning-particle dynamics. For a given set of fixed parameters, the circular-orbit equations may admit more than one physically admissible unstable solution. In the parameter range considered below, two such solution pairs, $(E_{\rm near}, r_0^{\rm near})$ and $(E_{\rm far}, r_0^{\rm far})$, are obtained. These solutions are distinguished by their radial locations, with $r_0^{\rm near} < r_0^{\rm far}$: the smaller-radius solution is referred to as the near-horizon branch, whereas the larger-radius solution defines the far-horizon branch. Thus, E is determined separately for each branch and is recalculated at every parameter point used in the numerical analysis.

III. VIOLATION OF THE CHAOS BOUND

For an appropriate range of parameters, this black hole spacetime admits a double photon sphere structure [46]. For a massive spinning particle, the spin–curvature coupling modifies the equations of motion and, consequently, the effective potential governing the radial dynamics. In the following numerical analysis, we employ the metric function given in Eq. (7) and define the dimensionless spin parameter as $s = S/M = \pm\tilde{S}/(mM)$. We set $M = 1$, so that S and s have the same numerical value. Unless otherwise specified, we take $\alpha = -0.0345$, $\beta = 1.05$, $Q = -0.01$, and $L = 6.00$, and define $\Delta_{\lambda\kappa} = \lambda^2 - \kappa^2$.

For each set of parameters, the corresponding unstable circular orbit solutions are obtained from the circular orbit conditions described in Sec. II.C. As an illustrative example, Table 1 lists representative values of $(r_0, E, \lambda, \kappa)$ for the two unstable circular orbit branches. The event horizon radius and the inner and outer photon sphere radii r_{ph} of the same black hole background are also included to enable direct comparison with the radial locations of the two unstable circular orbits r_0. Both orbits lie outside the event horizon. The circular orbit conditions yield two distinct solutions, $(E, r_0) = (0.81542, 0.61770)$ and $(1.39044, 2.58083)$, corresponding to the near-horizon and far-horizon branches, respectively. Because the two branches belong to the same black hole background, they share the same surface gravity, $\kappa = 0.08305$, whereas their orbital radii, conserved energies, and LEs differ. In particular, the near-horizon branch satisfies $\lambda < \kappa$, whereas the far-horizon branch satisfies $\lambda > \kappa$, indicating that the two branches exhibit different local instability behavior for the same horizon scale.

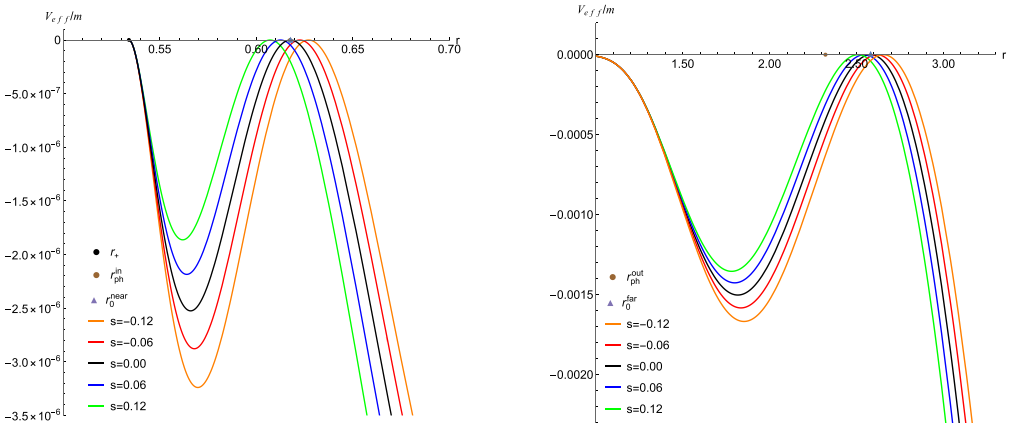
Table 1. Representative values for the near- and far-horizon unstable circular orbits in the spinless case ($S = 0$), with $M = 1$, $\alpha = -0.0345$, $\beta = 1.05$, $Q = -0.01$, and $L = 6.00$. The corresponding inner and outer photon-sphere radii are included for comparison. The event horizon radius is $r_+ = 0.53401$.

Branch	$r_{\rm ph}^{\rm in/out}$	r_0	E	λ	κ
Near-horizon branch	0.61747	0.61770	0.81542	0.06067	0.08305
Far-horizon branch	2.32097	2.58083	1.39044	0.12149	0.08305

Figure 1 shows the radial dependence of the effective potential for different spin configurations in the near- and far-horizon regions. For each spin value, the corresponding unstable circular orbit is located at a local maximum of the effective potential, and these maxima define the near- and far-horizon branches. Figure 1(a) displays the near-horizon branch, whereas Fig. 1(b) shows the corresponding far-horizon branch. For the parameter values specified above, the locations of the event horizon and the inner and outer photon spheres are marked in Fig. 1. The unstable circular orbits for different spin values are identified by the local maxima of the corresponding effective potentials. Representative values for the spinless case are given in Table 1. For $S = 0$, the characteristic radii satisfy $r_+ < r_{\rm ph}^{\rm in} < r_0^{\rm near} < r_{\rm ph}^{\rm out} < r_0^{\rm far}$. In the spinless configuration, the near-horizon unstable orbit lies very close to the inner photon sphere, whereas the far-horizon unstable orbit is located outside the outer photon sphere. However, the two photon spheres do not coincide with the corresponding unstable circular orbits of the massive particle, indicating that there is no simple one-to-one correspondence between them. The two orbit branches nevertheless occupy distinct radial regions associated with the double photon sphere geometry. Importantly, both unstable branches are already present in the spinless case, indicating that their existence is not generated by spin-curvature coupling. Moreover, because the two branches belong to the same black hole background, the associated surface gravity is identical, and the difference between their LEs originates from the different local radial dynamics around the corresponding unstable orbits. In particular, the effective potential has different local curvatures at the two maxima, while the exponent is determined by the local curvature of the effective potential at an unstable circular orbit. The difference in the local curvature of the effective potential therefore provides a dynamical explanation for the distinct LEs of the two branches.

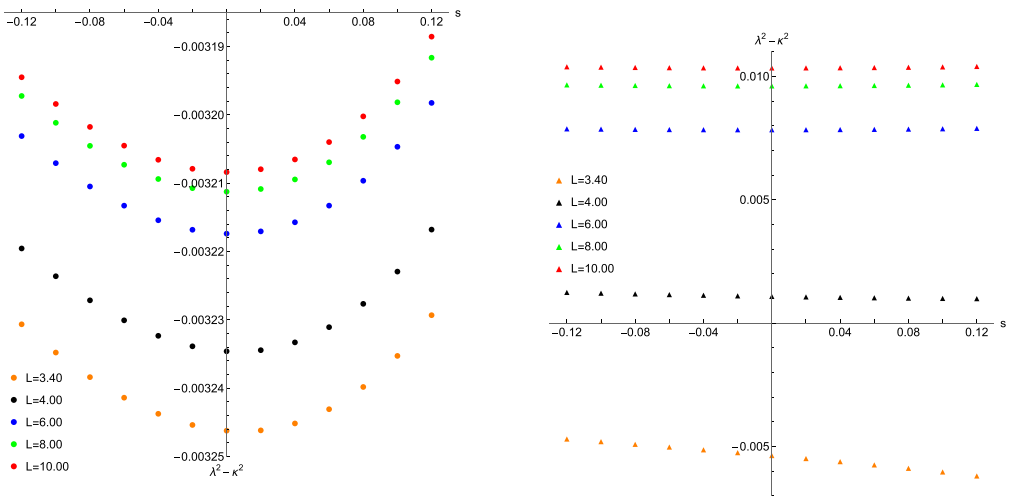
In the following analysis, we numerically evaluate the particle LE and the surface gravity of the black hole using Eqs. (38) and (9), respectively. The corresponding results, shown in Figs. 2–7, are used to investigate whether the chaos bound is satisfied in the black hole spacetime considered here.

Figure 2 shows the dependence of $\Delta_{\lambda\kappa}$ on the particle's spin. Because the black-hole background is fixed in this comparison, the surface gravity κ remains



(a) Near-horizon branch. (b) Far-horizon branch.

Fig. 1. (color online) Radial effective potential of the spinning particle as a function of the radial coordinate. In panel (a), $r_0^{\rm near}$ for $S=0$ is extremely close to the inner photon sphere radius $r_{\rm ph}^{\rm in}$. Consequently, the corresponding markers nearly overlap at the scale of the figure, and the photon sphere marker is largely obscured by the triangular marker denoting the spinless particle orbit.



(a) Near-horizon branch. (b) Far-horizon branch.

Fig. 2. (color online) Dependence of $\Delta_{\lambda\kappa}$ on particle spin for unstable circular orbits.

unchanged. Thus, the variation in $\Delta_{\lambda\kappa}$ directly reflects the corresponding variation in the orbital LE. To remain within a regime in which the pole–dipole approximation is expected to be reliable, we restrict the physical discussion in Fig. 2 to $|s|\leq 0.12$. For all retained circular-orbit solutions, the normalized spin length S remains small compared with the background scales. In particular, we find

$$\frac{|S|}{M}\leqslant 0.12,\quad \frac{|S|}{r_0}\leqslant 0.04784,\quad \frac{|S|}{\mathcal{R}_K}\leqslant 0.06418, \tag{42}$$

where

$$\mathcal{R}_K=K^{-1/4},\quad K=R_{\mu\nu\rho\sigma}R^{\mu\nu\rho\sigma}, \tag{43}$$

R_K provides a local curvature length scale inferred from the Kretschmann scalar. The small values of these ratios support the consistency of the retained configurations with the small-spin regime required by the pole–dipole description. We also examined the causal character of the corresponding circular worldlines under the TD condition. Because the four-velocity is generally not parallel to the four-momentum under this condition, normalization of the momentum alone does not guarantee that the particle worldline is timelike. We therefore directly evaluate the causal character of these worldlines

$$g_{\mu\nu}u^\mu u^\nu<0. \tag{44}$$

For a circular equatorial orbit, $u^r=u^\theta=0$, and the timelike condition becomes

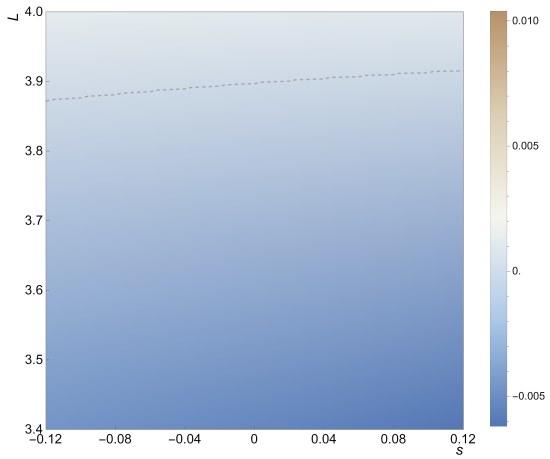


Fig. 3. (color online) Distribution of $\Delta_{\lambda\kappa}$ over the (S,L) parameter plane for the far-horizon branch. The dashed line denotes the critical boundary, $\Delta_{\lambda\kappa}=0$.

$$-f(r_0)(u^t)^2+r_0^2(u^\phi)^2<0. \tag{45}$$

Using the coordinate angular velocity $\dot{\phi}=\dfrac{\mathrm{d}\phi}{\mathrm{d}t}=\dfrac{u^\phi}{u^t}$, this condition can equivalently be written as

$$-f(r_0)+r_0^2\dot{\phi}^2<0. \tag{46}$$

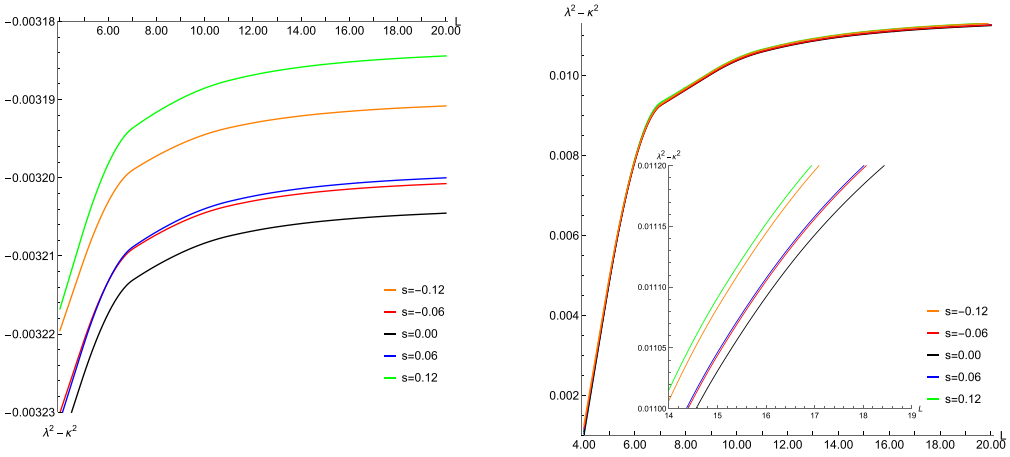
For all spin values shown in Fig. 2, we find

$$-0.04874\leqslant -f(r_0)+r_0^2\dot{\phi}^2\leqslant -0.04427. \tag{47}$$

Hence, all circular worldlines retained in the physical analysis are timelike, and no superluminal configurations are included in the assessment of chaos-bound behavior.

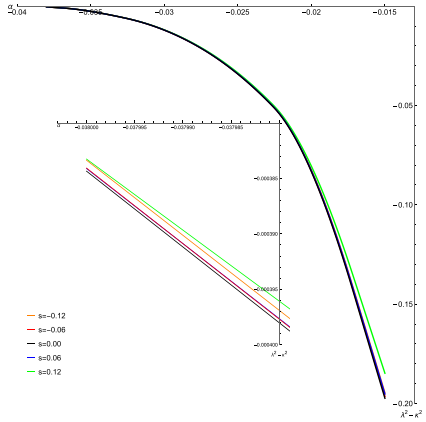
Figure 2(a) displays the spin dependence of $\Delta_{\lambda\kappa}$ for the near-horizon branch. In this branch, $\Delta_{\lambda\kappa}$ reaches a minimum near the spinless configuration and increases as the spin deviates from zero in either direction. Throughout the spin range considered, however, $\Delta_{\lambda\kappa}<0$, indicating that the near-horizon branch remains in the bound-satisfying regime. The spin dependence is asymmetric with respect to positive and negative spin, reflecting the dependence of the spin–curvature interaction on the relative orientation between the particle spin and the orbital angular momentum. Moreover, at fixed spin, $\Delta_{\lambda\kappa}$ increases monotonically with the total angular momentum. Since the surface gravity is fixed, this trend corresponds to an increase in the orbital LE with the total angular momentum. Over the parameter range considered, the variation with the total angular momentum is more pronounced than the spin-induced correction. The far-horizon branch exhibits qualitatively different behavior, as shown in Fig. 2(b). For all configurations retained in the physical spin range, $\lambda^2>\kappa^2$, and the corresponding unstable circular orbits therefore lie in the chaos-bound-violation regime according to the local orbital-instability criterion adopted here. As in the near-horizon case, $\Delta_{\lambda\kappa}$ increases monotonically with the total angular momentum. Its dependence on the particle spin, however, is not universally monotonic and varies with the total angular momentum. In particular, for $L=4.00$, the minimum is shifted toward positive spin, whereas for $L=6.00$, 8.00, and 10.00, it lies close to the spinless configuration. Thus, the far-horizon branch does not exhibit a universal increase with increasing spin magnitude.

These results show that spin–curvature coupling modifies the local instability of unstable circular orbits in a branch- and parameter-dependent manner. Changing the particle spin modifies the radial effective potential and simultaneously shifts the location of the unstable circular orbit. Since the LE is determined by the local curvature of the effective potential evaluated at the corresponding orbit, these effects can compete and need not produce a monotonic dependence on spin. The asymmetry between

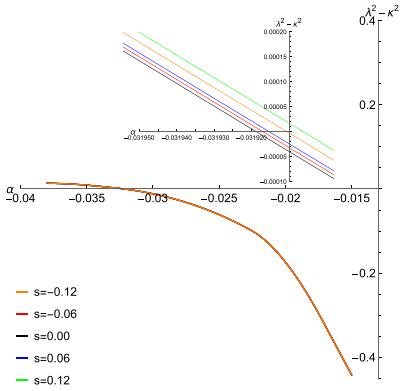


(a) Near-horizon branch. (b) Far-horizon branch.

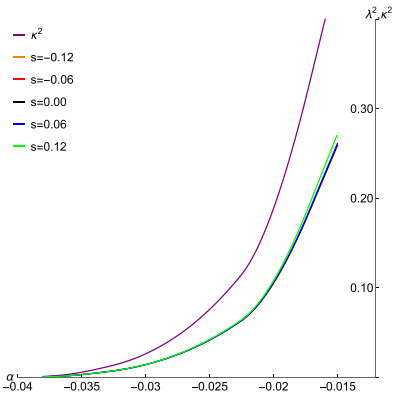
Fig. 4. (color online) Dependence of $\Delta_{\lambda\kappa}$ on total angular momentum for unstable circular orbits.



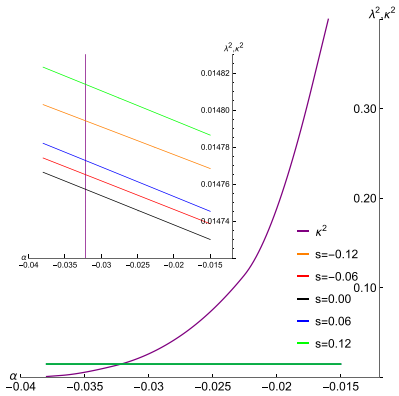
(a) Near-horizon branch.



(b) Far-horizon branch.



(c) Near-horizon branch.



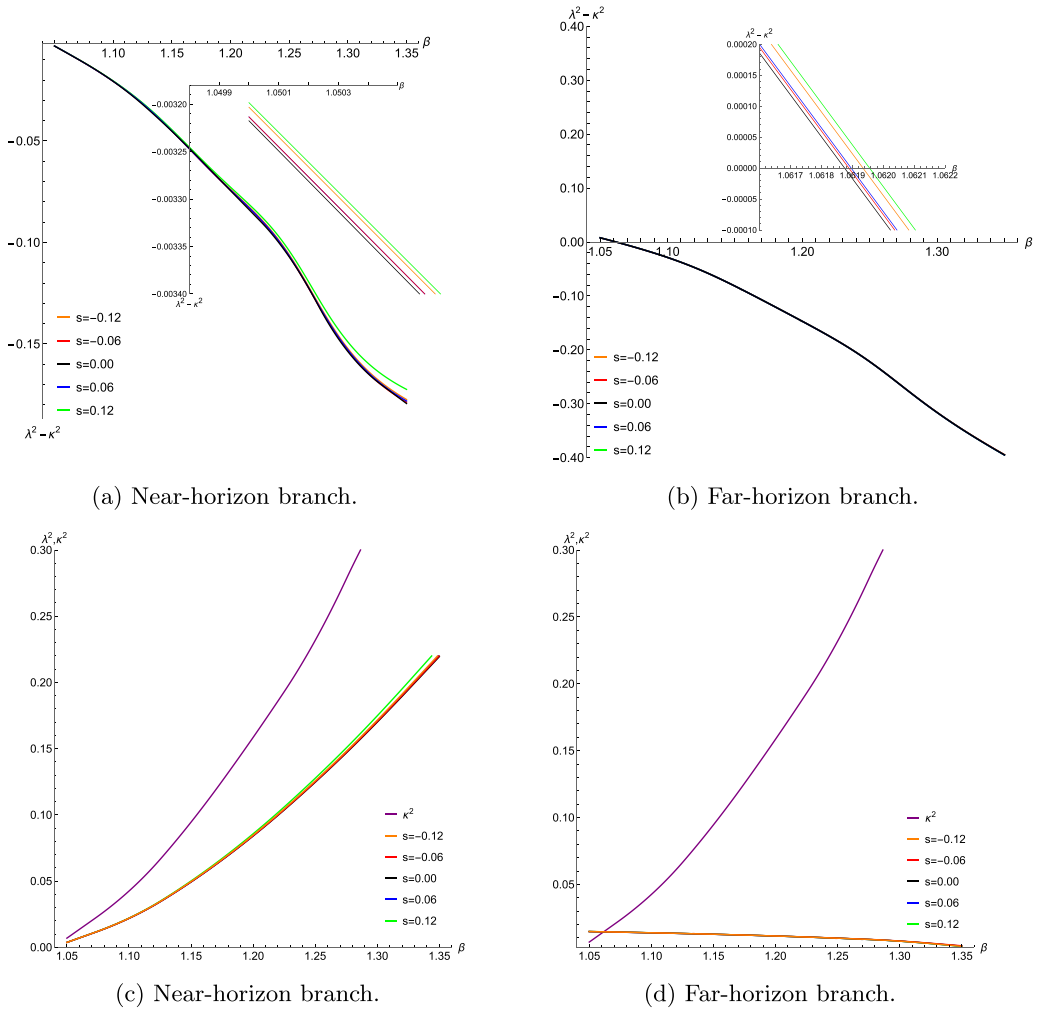
(d) Far-horizon branch.

Fig. 5. (color online) Dependence of $\Delta_{\lambda\kappa}$, the LE, and the surface gravity on the coupling parameter α.

positive and negative spin reflects the orientation dependence of the spin–curvature interaction. Although both the near-horizon and far-horizon branches correspond to local maxima of the effective potential in the same black hole background, their behavior relative to the surface-gravity scale differs markedly. The near-horizon branch remains in the bound-satisfying regime, whereas the far-horizon branch lies in the violation regime for the parameter values considered here. The occurrence of an unstable circular orbit is therefore not, by itself, sufficient to determine whether the exponent exceeds the surface gravity. Instead, the result depends on the orbital branch and on the local structure of the effective potential around the corresponding orbit.

The preceding one-dimensional analysis shows that, within the physically allowed spin range considered in this work, the near-horizon branch always satisfies $\Delta_{\lambda\kappa} < 0$ and exhibits no critical behavior. We therefore focus on the critical behavior of the far-horizon branch in the (S, L) parameter plane. Figure 3 shows the distribution of $\Delta_{\lambda\kappa}$ for the far-horizon branch; the dashed line denotes the critical boundary $\Delta_{\lambda\kappa} = 0$. As the spin increases, the critical angular momentum exhibits a gradual overall increase, indicating that particle spin shifts the critical angular momentum at which $\lambda = \kappa$ is reached, although this shift remains relatively small over the spin range considered. Thus, including spin does not alter the existence of the far-horizon branch but instead quantitatively modifies its chaos-bound behavior by shifting the corresponding critical boundary.

Figure 4 shows the dependence of $\Delta_{\lambda\kappa}$ on the particle's total angular momentum. The variation of $\Delta_{\lambda\kappa}$ in this figure also directly reflects the corresponding variation of the orbital LE. Figure 4(a) corresponds to the near-horizon branch. For all spin configurations considered, $\Delta_{\lambda\kappa}$ increases monotonically with the total angular momentum. This increase is relatively rapid in the low-angular-momentum regime and becomes progressively weaker as the angular momentum grows, indicating a tendency toward saturation. Nevertheless, throughout the entire parameter range considered, the exponent remains below the surface gravity; thus, the near-horizon branch always satisfies the chaos bound. A comparison among different spin configurations shows that, at fixed



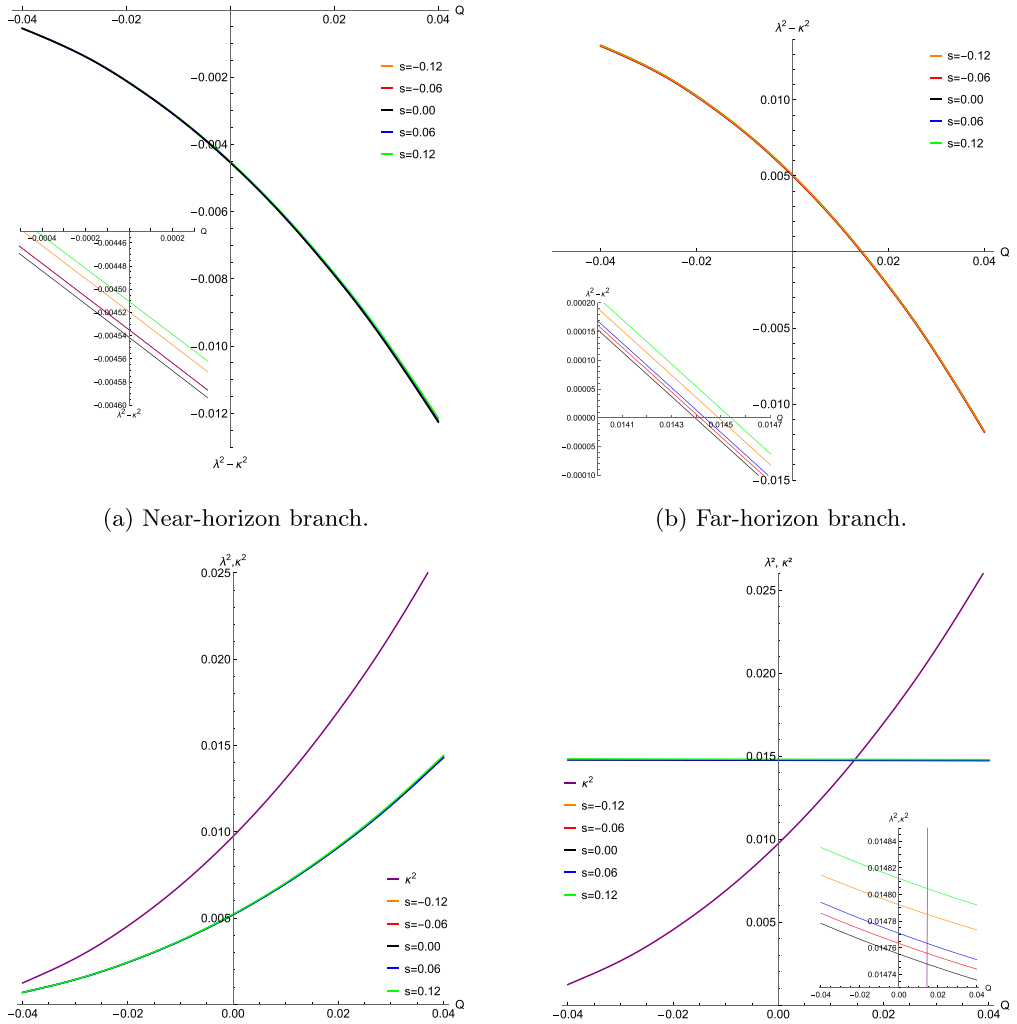
(a) Near-horizon branch. (b) Far-horizon branch.

(c) Near-horizon branch. (d) Far-horizon branch.

Fig. 6. (color online) Dependence of $\Delta_{\lambda\kappa}$, the LE, and the surface gravity on the coupling parameter β.

total angular momentum, the spinless configuration yields the smallest value of $\Delta_{\lambda\kappa}$ and hence the smallest LE, since the surface gravity is fixed in this comparison. This behavior applies to the near-horizon branch over the parameter range shown here and should not be regarded as a general dependence on spin for both orbital branches. The deviation from the spinless case generally increases with spin magnitude, indicating that the spin–curvature coupling modifies the sensitivity of the unstable circular orbit to radial perturbations. Moreover, for a given spin magnitude, positively aligned spins yield systematically larger values of $\Delta_{\lambda\kappa}$, and hence larger LEs, than negatively aligned spins over the parameter range shown for the near-horizon branch. This asymmetry reflects the dependence of the spin–curvature interaction on the relative orientation between the particle spin and the orbital angular momentum.

Figure 4(b) displays the corresponding results for the far-horizon branch. As in the near-horizon case, $\Delta_{\lambda\kappa}$ increases monotonically with the total angular momentum, with a pronounced increase at small angular momentum followed by milder variation in the large-angular-momentum regime. In contrast to the near-horizon branch, however, all configurations considered satisfy $\Delta_{\lambda\kappa} > 0$ and therefore lie in the chaos-bound-violation regime according to the local orbital-instability criterion adopted here. The separation among the curves associated with different spin parameters is relatively small for the far-horizon branch. Thus, in the parameter range considered, the variation with total angular momentum is considerably more pronounced than the spin-induced correction. For $L = 6.00$, 8.00, and 10.00, the spinless configuration lies close to the minimum with respect to spin. For $L = 4.00$, however, the ordering changes, consistent with the behavior shown in Fig. 2(b), where the minimum is shifted toward positive spin. Therefore, the spin dependence of the far-horizon branch cannot be characterized by a universal monotonic increase with spin magnitude or by a fixed ordering between positive and negative spins over the entire angular-momentum range. This nonmonotonic behavior can be understood from the spin–curvature coupling, which changes both the location of the unstable circular orbit and the local curvature of the effective potential at that orbit. Since these two effects vary with both S and L,



(a) Near-horizon branch. (b) Far-horizon branch.

(c) Near-horizon branch. (d) Far-horizon branch.

Fig. 7. (color online) Dependence of $\Delta_{\lambda\kappa}$, the LE, and the surface gravity on the primary hair Q.

their combined contribution to the orbital LE need not be monotonic in the particle spin.

Taken together, these results show that both the total angular momentum and the spin–curvature coupling affect the local radial instability, although the dependence on the total angular momentum is more pronounced over the parameter range considered. Increasing the total angular momentum increases $\Delta_{\lambda\kappa}$, whereas the particle spin introduces a comparatively smaller orientation-dependent correction. More importantly, although both branches correspond to unstable circular orbits in the same double-photon-sphere background, they exhibit qualitatively different behaviors relative to the surface gravity scale. The near-horizon branch remains in the bound-satisfying regime, whereas the far-horizon branch lies in the bound-violating regime for the parameter values considered here. This distinction demonstrates that whether the LE exceeds the surface gravity depends not only on the existence of an unstable circular orbit but also on the orbital branch and the local structure of the effective potential around the corresponding orbit.

Figure 5 shows the dependence of $\Delta_{\lambda\kappa}$, the squared LE, and the squared surface gravity on the coupling parameter α for the near- and far-horizon branches. For the near-horizon branch, shown in Fig. 5(a), $\Delta_{\lambda\kappa}$ decreases monotonically as the coupling parameter increases. Nevertheless, all curves remain below the horizontal axis throughout the parameter range considered, indicating that the near-horizon branch remains in the bound-satisfying regime. Moreover, $\Delta_{\lambda\kappa}$ becomes more negative as the coupling increases, so these configurations move farther away from the critical value $\Delta_{\lambda\kappa}=0$. At a fixed value of the coupling parameter, different spin configurations yield slightly different values of $\Delta_{\lambda\kappa}$. Because the surface gravity is the same for different particle spins at fixed background parameters, this splitting reflects the corresponding spin dependence of the orbital LE. The differences among the spin configurations remain small over

the parameter range considered, although they become somewhat more visible as the coupling parameter increases. For the far-horizon branch, shown in Fig. 5(b), $\Delta_{\lambda\kappa}$ exhibits a similar decreasing dependence on the coupling parameter. Unlike in the near-horizon case, $\Delta_{\lambda\kappa}$ is positive for sufficiently negative values of α and crosses zero as the coupling parameter increases. The corresponding critical coupling depends slightly on the particle spin. Thus, the far-horizon branch transitions from the bound-violating regime to the bound-satisfying regime across this critical value. The hierarchy of the curves for different spin configurations remains unchanged, and their separation remains relatively small throughout the displayed range, as shown more clearly in the inset. At fixed coupling, the particle spin therefore produces only a small correction to $\Delta_{\lambda\kappa}$ and slightly shifts the critical coupling, whereas the overall variation with the coupling parameter is much more pronounced. Because varying a black-hole coupling parameter changes the background geometry, both the orbital LE and the surface gravity may vary. Therefore, the decrease in $\Delta_{\lambda\kappa}$ should not by itself be interpreted as a decrease in the orbital instability.

To clarify the origin of the variation in $\Delta_{\lambda\kappa}$, Figs. 5(c) and 5(d) separately show the variations of λ^2 and κ^2, corresponding to the squared orbital-instability and surface-gravity scales, respectively. As the coupling parameter increases, κ^2 increases for both orbital branches, whereas λ^2 exhibits opposite trends for the two branches. For the near-horizon branch, λ^2 also increases, but more slowly than κ^2, resulting in a decrease in $\Delta_{\lambda\kappa}$. Thus, the decrease in $\Delta_{\lambda\kappa}$ in this branch does not correspond to a weakening of the orbital instability. By contrast, for the far-horizon branch, the orbital-instability scale decreases while the surface-gravity scale increases. These two effects therefore act together to reduce $\Delta_{\lambda\kappa}$. The intersection of the λ^2 and κ^2 curves corresponds to $\lambda^2 = \kappa^2$ and thus marks the critical point separating the bound-satisfying and bound-violating regimes. These results show that the response of the orbital instability to the coupling parameter is branch dependent and further illustrate why the behavior of $\Delta_{\lambda\kappa}$ should be distinguished from that of the LE itself.

Figure 6 illustrates the dependence of $\Delta_{\lambda\kappa}$, the squared LE, and the squared surface gravity on the coupling parameter β for the near- and far-horizon branches. For the near-horizon branch, as shown in Fig. 6(a), $\Delta_{\lambda\kappa}$ exhibits an overall decrease as the coupling parameter increases. Although the curves approach the critical value $\Delta_{\lambda\kappa} = 0$ in the lower-coupling region, they remain below the critical line throughout the parameter range considered. Therefore, the near-horizon branch remains in the bound-satisfying regime. At a fixed value of the coupling parameter, different spin configurations yield slightly different values of $\Delta_{\lambda\kappa}$. Since the surface gravity is independent of the particle spin at fixed background parameters, this splitting reflects the corresponding spin dependence of the orbital LE. The separation among the spin curves gradually decreases as the coupling parameter increases, indicating that the spin-induced correction to $\Delta_{\lambda\kappa}$ becomes less pronounced over the displayed range. For the far-horizon branch, shown in Fig. 6(b), $\Delta_{\lambda\kappa}$ also decreases as the coupling parameter increases. In contrast to the near-horizon branch, $\Delta_{\lambda\kappa}$ is positive below a critical coupling and crosses zero as the parameter increases. The corresponding critical coupling depends slightly on the particle spin. Thus, the far-horizon branch changes from the bound-violating regime to the bound-satisfying regime across this critical value. The separation among the curves associated with different spin configurations remains relatively small, showing that spin produces only a small shift in the critical value over the parameter range considered.

Figures 6(c) and 6(d) provide a separate comparison of λ^2 and κ^2 as the coupling constant β varies. As this coupling constant increases, κ^2 increases for both orbital branches, whereas the response of λ^2 is branch dependent. For the near-horizon branch, λ^2 increases more slowly than κ^2, so that $\Delta_{\lambda\kappa}$ decreases even though the orbital instability itself becomes stronger. For the far-horizon branch, λ^2 decreases while κ^2 increases, and the two effects jointly drive $\Delta_{\lambda\kappa}$ downward. In this branch, the crossing of the λ^2 and κ^2 curves identifies the critical condition $\lambda^2 = \kappa^2$ and marks the transition from the bound-violating to the bound-satisfying regime. Thus, although $\Delta_{\lambda\kappa}$ decreases for both branches, the underlying evolution of the orbital instability is qualitatively different.

Figure 7 shows the dependence of $\Delta_{\lambda\kappa}$ on the primary hair Q. For the near-horizon branch, as shown in Fig. 7(a), $\Delta_{\lambda\kappa}$ decreases monotonically as the primary hair increases from negative to positive values and remains negative throughout the parameter range considered. The chaos bound is therefore always satisfied for this branch. The separation among the curves for different spin values also becomes smaller as the primary hair decreases, indicating that the spin-dependent correction becomes less pronounced. For the far-horizon branch, as shown in Fig. 7(b), $\Delta_{\lambda\kappa}$ likewise decreases with increasing primary hair but initially lies in the bound-violating regime with $\Delta_{\lambda\kappa} > 0$. As the primary hair increases, it crosses the critical line $\Delta_{\lambda\kappa} = 0$ and enters the bound-satisfying regime. Figures 7(c) and 7(d) show the branch-dependent response: κ^2 increases for both branches, whereas λ^2 increases for the near-horizon branch but decreases for the far-horizon branch. In the former case, the increase in λ^2 is weaker than that in κ^2, so that $\Delta_{\lambda\kappa}$ still decreases despite the strengthening of the orbital instability. In the latter case, the decrease in λ^2 and the increase in κ^2 act together to reduce $\Delta_{\lambda\kappa}$. Their intersection, $\lambda^2 = \kappa^2$, marks the transition from the bound-violating to the bound-satisfying regime. Thus, although increasing the primary hair suppresses $\Delta_{\lambda\kappa}$ for both orbital branches, the underlying response of the orbital instability remains branch dependent.

IV. CONCLUSION AND DISCUSSION

In this paper, we investigated the orbital instability of spinning test particles in a spherically symmetric black hole spacetime and its relation to the classical chaos bound. In the parameter region considered, the radial effective potential develops two local maxima, corresponding to two branches of unstable circular orbits. Although both branches are radially unstable, their LEs exhibit different behaviors with respect to the same surface gravity. The near-horizon branch generally satisfies the bound, whereas the far-horizon branch can enter a regime in which the LE exceeds the surface gravity scale. This indicates that whether the local instability rate exceeds the surface gravity depends not only on the radial instability of the orbit itself but also on the orbital location and the local structure of the effective potential near the corresponding extremum. Particle spin shifts the locations of the unstable orbits and modifies their local instability rates through spin–curvature coupling, but it does not generate the two-branch structure in the parameter range studied here. The coupling parameters and primary hair further modify the relation between the orbital-instability and surface gravity scales through their effects on the background geometry and the effective potential. In particular, as these parameters and primary hair increase, κ^2 increases for both orbital branches, whereas λ^2 increases for the near-horizon branch but decreases for the far-horizon branch. This branch-dependent behavior also shows that the variation of $\Delta_{\lambda\kappa}$ results from the combined changes in the Lyapunov exponent and surface gravity and should not be identified with the variation of the orbital instability alone.

For the far-horizon branch, the occurrence of $\lambda^2_{\rm far} > \kappa^2$ means, within the criterion adopted here and in related studies of classical particle dynamics, that the local radial instability rate around the orbit exceeds the surface gravity scale. It can therefore be regarded as a violation of the classical particle-orbit bound $\lambda^2 \le \kappa^2$. We stress, however, that this violation refers to the local radial perturbation of an unstable circular orbit and does not imply the presence of global classical chaos in the full phase space. Previous studies of classical particle dynamics in rotating black hole backgrounds have shown that black hole rotation and the particle orbital angular momentum can modify the effective potential, the locations of unstable orbits, and the corresponding LEs. Different magnitudes and orientations of the particle angular momentum can further alter the relation between the orbital instability rate and the surface gravity, allowing the bound to be violated in certain parameter regions. In contrast to those rotating backgrounds, the two unstable branches found here arise from two distinct maxima of the radial effective potential in the same static and spherically symmetric spacetime, and both are already present in the spinless limit. Thus, even in the absence of black hole rotation, different unstable orbits in the same static background can exhibit different behaviors with respect to the same surface gravity scale. Finally, the LE considered in this work characterizes the local growth of linear radial perturbations around classical unstable circular orbits and is therefore not the same quantity as the quantum LE extracted from OTOCs and associated with quantum information scrambling. Consequently, the condition $\lambda^2 > \kappa^2$ found here should not be directly identified with a violation of the MSS chaos bound.

References

[1] J. Maldacena, S. H. Shenker, and D. Stanford, JHEP **08**, 106 (2016)
[2] S. H. Shenker and D. Stanford, JHEP **1412**, 046 (2014)
[3] S. H. Shenker and D. Stanford, JHEP **1403**, 067 (2014)
[4] S. H. Shenker and D. Stanford, JHEP **1505**, 132 (2015)
[5] V. Jahnke, K. Y. Kim, and J. Yoon, JHEP **1905**, 037 (2019)
[6] R. R. Poojary, JHEP **2003**, 048 (2020)
[7] Y. Liu and A. Raju, JHEP **2012**, 027 (2020)
[8] K. Hashimoto and N. Tanahashi, Phys. Rev. D **95**, 024007 (2017)
[9] Q. Q. Zhao, Y. Z. Li, and H. Lü, Phys. Rev. D **98**, 124001 (2018)
[10] Y. Q. Lei and X. H. Ge, Phys. Rev. D **105**, 084011 (2022)
[11] Y. Q. Lei and X. H. Ge, Phys. Lett. B **856**, 138929 (2024)
[12] Y. Q. Lei, X. H. Ge, and C. Ran, Phys. Rev. D **104**, 046020 (2021)
[13] Y. Q. Lei and X. H. Ge, Phys. Rev. D **107**, 106002 (2023)
[14] N. Kan and B. Gwak, Phys. Rev. D **105**, 026006 (2022)
[15] B. Gwak, N. Kan, B. H. Lee *et al*., JHEP **2209**, 026 (2022)
[16] J. Park and B. Gwak, JHEP **2404**, 023 (2024)
[17] H. Lee and B. Gwak, Phys. Rev. D **112**, 046018 (2025)
[18] H. Lee and B. Gwak, arXiv: 2510.16479[gr-qc]
[19] K. Hashimoto, K. Murata, N. Tanahashi *et al*., Phys. Rev. D **106**, 126010 (2022)
[20] K. Hashimoto and K. Sugiura, Phys. Rev. D **107**, 066005 (2023)
[21] D. Giataganas, Fortsch. Phys. **70**, 2200001 (2022)
[22] C. H. Gao, D. Y. Chen, C. Y. Yu *et al*., Phys. Lett. B **833**, 137343 (2022)
[23] K. Li, D. Z. Ma, and Z. M. Xu, Phys. Lett. B **860**, 139164 (2025)
[24] D. Y. Chen and C. H. Gao, New J. Phys. **24**, 123014 (2022)
[25] S. Jeong, B. H. Lee, H. Lee *et al*., Phys. Rev. D **107**, 104037 (2023)
[26] P. Dutta, K. L. Panigrahi, and B. Singh, JHEP **02**, 043 (2025)
[27] A. Fayyaz, G. Abbas, M. B. Asfour *et al*., Phys. Lett. B **871**, 139965 (2025)
[28] Y. Xie, J. Wang, and B. Tang, Phys. Dark. Univ **42**, 101271 (2023)
[29] F. H. Lü, J. Tao, and P. Wang, JCAP **1812**, 036 (2018)
[30] X. B. Guo, K. K. Liang, B. R. Mu *et al*., Chin. Phys. C **45**,

023115 (2021)
[31] B. Singh, N. Padhi, and R. R. Nayak, Eur. Phys. J. C **85**, 570 (2025)
[32] R. Pourkhodabakhshi, Phys. Rev. D **112**, 064085 (2025)
[33] T. V. Targema, K. Bamba, R. Ali *et al*., Phys. Rev. D **113**, 104056 (2026)
[34] T. V. Targema, K. Bamba, and U. Zafar, arXiv: 2605.26829[hep-th]
[35] T. Morita, Eur. Phys. J. C **80**, 331 (2020)
[36] S. Dalui, B. R. Majhi, P. Mishra, Phys. Lett. B **788**, 486 (2019)
[37] E. Gallo and T. Mädler, Eur. Phys. J. C **85**, 299 (2025)
[38] C. Yang, D. Y. Chen, and Y. Liu, JHEP **04**, 205 (2026)
[39] X. Li, B. B. Chen, and G. P. Li, arXiv: 2604.03914[gr-qc]
[40] G. Z. Guo, X. Jiang, P. Wang *et al*., Phys. Rev. D **105**, 124064 (2022)
[41] G. Z. Guo, Y. H. Lu, P. Wang *et al*., Phys. Rev. D **107**, 124037 (2023)
[42] Y. Q. Chen, P. Wang, and H. T. Yang, Phys. Rev. D **110**, 044020 (2024)
[43] X. J. Wang, Y. Meng, X. M. Kuang *et al*., Phys. Rev. D **112**, 124016 (2025)
[44] P. G. S. Fernandes, Phys. Rev. D **103**, 104065 (2021)
[45] C. Charmousis, P. G. S. Fernandes, and M. Hassaine, Phys. Rev. D **111**, 124008 (2025)
[46] R. A. Konoplya, D. Ovchinnikov, and J. Schee, Phys. Rev. D **113**, 024059 (2026)
[47] H. Lu and Y. Pang, Phys. Lett. B **809**, 135717 (2020)
[48] R. Hojman and S. Hojman, Phys. Rev. D **15**, 2724 (1977)
[49] A. A. Deriglazov and W. G. Ramírez, Phys. Lett. B **779**, 210 (2018)
[50] W. Tulczyjew, Acta Physica Polonica **18**, 393 (1959)
[51] A. J. Hanson and T. Regge, Ann. Phys. **87**, 498 (1974)
[52] N. Zalaquett, S. A. Hojman, and F. A. Asenjo, Class. Quantum Grav. **31**, 085011 (2014)
[53] V. Cardoso, A. S. Miranda, E. Berti *et al*., Phys. Rev. D **79**, 064016 (2009)
[54] S. Y. Ciou, T. Hsieh, and D. S. Lee, JCAP **05**, 086 (2025)